



*Citation for published version:*

Fourneau, E., Arregi, J.A., Barrera, A., Nguyen, N.D., Bending, S., Sanchez, A., Uhlíř, V., Palau, A. & Silhanek, A.V. 2023, 'Microscale Metasurfaces for On-Chip Magnetic Flux Concentration', *Advanced Materials Technologies*, vol. 8, no. 16, 2300177. <https://doi.org/10.1002/admt.202300177>

*DOI:*

[10.1002/admt.202300177](https://doi.org/10.1002/admt.202300177)

*Publication date:*

2023

*Document Version*

Peer reviewed version

[Link to publication](#)

This is the peer reviewed version of the following article: Fourneau, E., Arregi, J.A., Barrera, A., Nguyen, N.D., Bending, S., Sanchez, A., Uhlíř, V., Palau, A. and Silhanek, A.V. (2023), Microscale Metasurfaces for On-Chip Magnetic Flux Concentration. *Adv. Mater. Technol.* 2300177, which has been published in final form at <https://doi.org/10.1002/admt.202300177>. This article may be used for non-commercial purposes in accordance with Wiley Terms and Conditions for Use of Self-Archived Versions. This article may not be enhanced, enriched or otherwise transformed into a derivative work, without express permission from Wiley or by statutory rights under applicable legislation. Copyright notices must not be removed, obscured or modified. The article must be linked to Wiley's version of record on Wiley Online Library and any embedding, framing or otherwise making available the article or pages thereof by third parties from platforms, services and websites other than Wiley Online Library must be prohibited.

## University of Bath

### Alternative formats

If you require this document in an alternative format, please contact:  
[openaccess@bath.ac.uk](mailto:openaccess@bath.ac.uk)



#### General rights

Copyright and moral rights for the publications made accessible in the public portal are retained by the authors and/or other copyright owners and it is a condition of accessing publications that users recognise and abide by the legal requirements associated with these rights.

#### Take down policy

If you believe that this document breaches copyright please contact us providing details, and we will remove access to the work immediately and investigate your claim.

# Microscale metasurfaces for on-chip magnetic flux concentration

Emile Fourneau <sup>1,2,\*</sup>, Jon Ander Arregi,<sup>3</sup> Aleix Barrera,<sup>4</sup> Ngoc Duy Nguyen,<sup>2</sup> Simon Bending,<sup>5</sup> Alvaro Sanchez,<sup>6</sup> Vojtěch Uhlíř,<sup>3,7</sup> Anna Palau,<sup>4</sup> and Alejandro V. Silhanek <sup>1,†</sup>

<sup>1</sup>*Experimental Physics of Nanostructured Materials, Q-MAT, CESAM, Université de Liège, B-4000 Sart Tilman, Belgium*

<sup>2</sup>*Solid-State Physics - Interfaces and Nanostructures, Q-MAT, CESAM, Université de Liège, B-4000 Sart Tilman, Belgium*

<sup>3</sup>*CEITEC BUT, Brno University of Technology, Purkyňova 123, 612 00 Brno, Czechia*

<sup>4</sup>*Institut de Ciència de Materials de Barcelona, ICMAB-CSIC, Campus UAB, 08193 Bellaterra, Spain*

<sup>5</sup>*Centre for Nanoscience and Nanotechnology, Department of Physics, University of Bath, Bath, BA2 7AY, United Kingdom*

<sup>6</sup>*Department of Physics, Universitat Autònoma de Barcelona, 08193, Bellaterra, Catalonia, Spain*

<sup>7</sup>*Institute of Physical Engineering, Brno University of Technology, Technická 2, 616 69 Brno, Czechia*

(Dated: March 14, 2023)

Magnetic metamaterials have demonstrated promising perspectives to improve the efficiency of magnetic flux concentrators. In this work, we investigate the effects of downscaling these devices for on-chip integration. We scrutinize the influence of the non-linear magnetic response of the ferromagnetic components, their magnetic irreversibility, the formation of magnetic domains, as well as the effects of geometry and size of the devices. Our results demonstrate that the implementation of metasurfaces at the microscale opens up new technological possibilities for enhancing the performance of magnetic field detectors and remotely charging small electric devices, thus paving the way towards new approaches in information and communication technologies.

PACS numbers: ....

## I. INTRODUCTION

In the current information and communication age, smart electronic systems, sensors, actuators, wireless, or remote monitoring technologies are experiencing a astonishing growth rate[1]. In particular, magnetic sensors have been implemented to achieve a wide diversity of operating functions in several applications. There are many approaches to sense magnetic fields[2, 3], based on different physical principles including Hall-effect, fluxgate, anisotropic magnetoresistance, magnetic tunnel junctions, SQUIDs, or nitrogen-vacancy centers. Although enormous progress has been made to improve their performances, considerable research effort is still needed to find new ideas enabling enhanced sensitivity, combined with low power, remote monitoring, or autonomous operation. An important problem for magnetic sensors arises from the combination of two technological trends: the need for very high sensitivities (detection and monitoring of gradually smaller magnetic fields) and the small volume available for the magnetic sensors in increasingly more densely integrated devices. These two trends sometimes lead to a conflicting strategy: reducing the volume of the sensor generally decreases its sensitivity, since the latter depends on the area threaded by the magnetic flux. A widely implemented solution for increasing magnetic concentration consists in placing the sensing area in the gap between two ferromagnetic strips [4–9]. However,

the potential of magnetic flux concentration for sensing devices is currently far from been fully exploited. This is due in part to the fact that concentration power has been so far studied only in simple ideal cases and can be further developed exploring other geometries, with more practical relevance. As with the sensors, further improvement of magnetic flux concentrators (MFC) could be beneficial for energy harvesters whose performance depends on the magnetic flux in the dedicated pick-up area [10, 11].

It has been demonstrated that by properly adapting the geometry of millimeter scale MFCs, a substantial amplification effect can be obtained with an optimal performance achieved in tanga-shaped concentrators [4, 12]. Later on, based on numerical simulations, Sun *et al.* [8] demonstrated that a triangle-shaped concentrator offers the widest linear working range and provides a competitive magnetic gain compared to other geometries. Recently, a new approach based on transformation optics techniques has been proposed to efficiently and homogeneously concentrate magnetic flux and collect energy from weak low-frequency magnetic fields at small scales, with the potential to radically improve the efficiency of the next-generation of sensors and magnetic harvesters[13]. Indeed, a metamaterial shell composed of concentric and equidistant funnels made of ferromagnetic foils surrounding a magnetic sensor, could enhance the magnetic field (for static and up to several kHz ac fields) in the sensing area, by a factor that depends on the shell radii ratio and the number of funnels [14]. This effect, however, has only been demonstrated in large-scale proof-of-principle experiments, e.g., bulky 3D concentrators or cylindrical systems [15, 16]. An important step forward consists in downscaling the concept of metama-

\* emile.fourneau@uliege.be

† asilhanek@uliege.be

terial shells to provide planar meso/micro-metasurfaces for integration in microscale on-chip devices, where the use of sensors and small harvesters is increasingly needed [17]. In addition, the proposed magnetic metamaterials have only been analyzed assuming that their components exhibit a linear response, without magnetic saturation and ignoring the irreversible response of real ferromagnetic materials. Scrutinizing the influence of these effects on the response of the magnetic flux concentration and quantifying their dependence on the geometry and size of the structure will further help the optimization of rational designs as well as identifying the operational limits of technologically-mature devices.

In this work, we carry out an experimental and numerical analysis of planar magnetic field concentrators representing miniaturized thin film versions of the designs proposed in Refs.[15, 16]. The numerical simulation includes modeling of magnetic domain structure effects in planar metasurfaces and assumes a realistic non-linear dependence of the magnetic permeability for the ferromagnetic components. We investigate the influence of the metasurface thickness and geometry in order to optimize the concentration gain and the range of the linear response. In addition, we investigate the influence of the applied field direction as well as the field homogeneity at the center of the devices. Experimental validation of the numerical results is obtained by exploiting a ferromagnetic sensor surrounded by the magnetic metamaterial.

## II. METHODS

### A. Modeling

The considered MFC consists of a flower-like structure as schematically presented in Fig. 1(a), where each petal of thickness  $t$  has the same opening angle  $\theta$  and is made of a soft ferromagnetic material. The inner and outer radii of the structure are  $R_i$  and  $R_o$ , respectively. Unless otherwise explicitly indicated, all simulations have been performed for a device with  $R_o = 5R_i = 5 \mu\text{m}$  and  $t = 80 \text{ nm}$ . This device is intended to concentrate the applied in-plane magnetic field  $B_a$  in the central region surrounded by the flower where a magnetic sensor will be located. The intensity of the concentrated field, labeled  $B_0$ , is the average of the field in a sphere of radius  $R_i/10$  centered at the geometrical center of the MFC. Note that the flower-like geometry and the presence of a magnetic multi-domain states in the ferromagnetic petals could produce a magnetic field  $\mathbf{B}_0$  that is non-collinear with  $\mathbf{B}_a$ . Therefore, a convenient figure of merit quantifying the concentration power of the device (so-called gain  $G$ ) is the ratio of the projection of the field at the center of the flower  $\mathbf{B}_0$  along the direction of the applied magnetic field,

$$G = \frac{\mathbf{B}_0 \cdot \mathbf{B}_a}{|B_a|^2}. \quad (1)$$

A regime in which  $G > 1$  will be referred to as concentrator, whereas for  $G < 1$  the device acts as a magnetic shield.

Micromagnetic modeling of the metamaterials were performed with the open-source MuMax3 program [18], a finite difference method to simulate the time- and space-dependent magnetization evolution by solving the Landau-Lifshitz-Gilbert (LLG) equation:

$$\frac{\partial \mathbf{m}}{\partial t} = \gamma \mathbf{H}_{eff} \times \mathbf{m} + \alpha \mathbf{m} \times \frac{\partial \mathbf{m}}{\partial t} \quad (2)$$

where  $\mathbf{m} = \mathbf{M}/M_s$  is the reduced magnetization,  $\gamma$  is the gyromagnetic ratio,  $\alpha$  is the damping constant and  $\mathbf{H}_{eff}$  is the effective field comprising the exchange, the Zeeman and the dipolar contributions. The modeled material is permalloy (Py) with magnetic saturation  $M_s = 860 \text{ kA/m}$ , exchange stiffness  $A_{ex} = 13 \text{ pJ/m}$ , and negligible magnetocrystalline anisotropy [19, 20]. The discretization cell size has been fixed to  $\sim 10 \text{ nm}$  in each direction. Even though this cell size exceeds the exchange length  $\lambda \sim 5 \text{ nm}$ , which could result in a loss of accuracy regarding the domain walls, we have confirmed in a device with  $R_o = 2.5 \mu\text{m}$  that the results remain nearly invariant for smaller cell sizes.

The micromagnetic simulations were compared to the response of a homogeneous ideal paramagnetic material (IPM) obtained through the same method as in Ref. [15] but extending it to account for a finite film thickness. The relative permeability of the IPM is set to  $\mu/\mu_0 = 10^5$ , with  $\mu$  being a temperature- and magnetic-field-independent constant. Under this assumption, the IPM will not exhibit any saturation field. Stationary Maxwell's equations in the absence of current are solved using a finite element method with the magnetostatic module of Comsol Multiphysics software. For each field configuration, a stationary solution is obtained with a relative accuracy of  $10^{-5}$ . The simulation box of lateral size  $8R_o$  (large enough to ensure an error due to field line confinement lower than 1%) is discretized using a tetrahedral mesh grid and imposed boundary conditions  $\mathbf{B} = \mathbf{B}_a$ .

### B. Experimental

Several 60-nm-thick Py flower-shaped MFCs with various designs have been fabricated on silicon substrates using radio-frequency sputtering deposition and electron-beam lithography techniques. The concentrators have a radii ratio  $R_o/R_i = 5$ , with an outer radius  $R_o$  of either 40 or 80  $\mu\text{m}$ , and a number of petals between 2 and 8. A scanning electron microscopy image of a four-petal structure is shown in Fig. 1(b). The exact thickness of the structure  $t = 61 \text{ nm}$  was obtained by atomic force microscopy (inset of panel (b)). A saturation magnetization of 712 kA/m was determined from magnetization hysteresis loop measurements of unpatterned Py thin

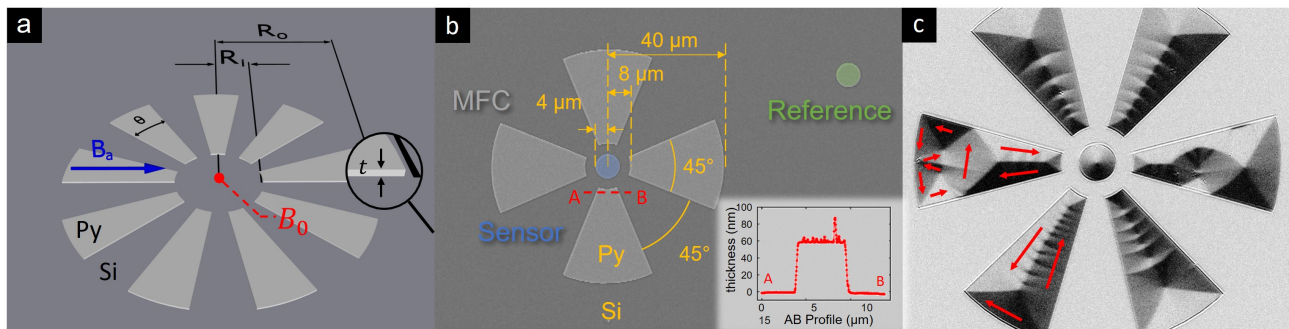


FIG. 1. (a) Sketch of the magnetic flux concentrator indicating the main geometrical parameters and the applied magnetic field orientation. (b) Scanning electron microscopy image of a four-petal MFC ( $R_o = 80 \mu\text{m}$ ) with a central disk-shaped magnetic sensor (blue coloured) and a reference sensor (in green). The inset shows a thickness line-profile obtained by atomic force microscopy. (c) MOKE image of a six-petal device ( $R_o = 80 \mu\text{m}$ ) in the demagnetized state. The perfect symmetry in the petal on the right hand side is broken by the presence of a small defect. The red arrows indicate the mean direction of the in-plane magnetic moment.

films using a Quantum Design SQUID magnetometer. The magnetic domains were visualized using a magneto-optical Kerr effect (MOKE) microscope from Evico magnetics in the longitudinal Kerr configuration using a  $50\times$  magnification objective lens [21]. MOKE images presented in this work are obtained employing background subtraction. In Fig. 1(c), a MOKE image corresponding to the demagnetized state is shown for a six-petal structure with an outer radius of  $R_o = 80 \mu\text{m}$ . Landau and diamond patterns as well as cross-tie domain walls are clearly visible. The domain orientation is indicated with red arrows for two of the petals. The central disk is made of Py and will serve as magnetic field sensor. The results presented in this work compile measurements performed in more than 15 devices and repeated on the same device several times.

### III. RESULTS AND DISCUSSION

#### A. Numerical investigation

Until now, numerical investigations of magnetic metamaterial-based flux concentrators have only been realized for macroscopic dimensions [14–16, 22]. In addition, the materials forming the concentrators have been assumed to be homogeneous, isotropic and linear. Neither the non-linear response nor the inherent irreversibility of the ferromagnetic hysteresis have been taken into consideration. In order to determine the impact of the magnetic domain distribution in a MFC, we compute the local reduced magnetization  $\mathbf{m}(\mathbf{r})$  in a six-petal 80-nm-thick concentrator and calculate the resulting stray field  $\mathbf{B}_s(\mathbf{r})$  induced at the center of the device, which in turn will define the concentration power of the device. The gain of the MFC is defined by Eq. (1) with the component of the field  $\mathbf{B}_0 = \mathbf{B}_s + \mathbf{B}_a$  at the center of the structure along the applied field direction. In Fig. 2(a),

the hysteresis cycle of  $B_s$  is plotted as a function of  $B_a$  whereas the calculated gain is shown in the inset.

We observe that the linear response of the concentrator (correspondingly resulting into a constant gain  $G$ ) takes place within a narrow magnetic field range highlighted by a blue (orange) shaded area for the ascending (descending) magnetic field sweep. Within this field range, the magnetic domains arrange themselves to form flux-closure patterns with a vortex core and/or a cross-tie wall separating two anti-parallel domains. The displacement of the magnetic vortex cores, as indicated by the black arrows in panels (c-e) of Fig. 2, provides the linear response. For high applied magnetic fields, the magnetic response saturates and the stray field remains almost constant ( $G \approx 1$ ). The observed slight decrease of  $B_s$  as the device reaches saturation is due to the fact that the petals perpendicular to  $\mathbf{B}_a$  generate a stray field in the opposite direction to the petals parallel to  $\mathbf{B}_a$ , thus tending to reduce the total stray field. Two important messages can be drawn from an analysis of Fig. 2: (i) the presence of magnetic domains severely reduces the field range for which the MFC can operate in the linear regime and (ii) the saturation field leads to a reduction of the gain.

In order to investigate the influence of the concentrator thickness, micromagnetic simulations have been performed for thicknesses varying from 40 to 100 nm, and for three different number of petals  $N_p = 4, 6, 8$ . The main findings are summarized in Fig. 3 where the gain calculated in the linear regime of a ferromagnetic device is compared with that predicted by the IPM model for thicknesses varying from 40 nm to 2  $\mu\text{m}$ . For reference, the performance of an infinitely tall cylindrical concentrator ( $t \rightarrow \infty$ ) is indicated by the right-pointing arrows. Note that MFCs of finite thicknesses have an improved gain compared to macroscopically thick ones. The reason for this is that thin devices are able to collect additional magnetic field lines from above and below the plane of the device. This enhancement is less pronounced as  $t$

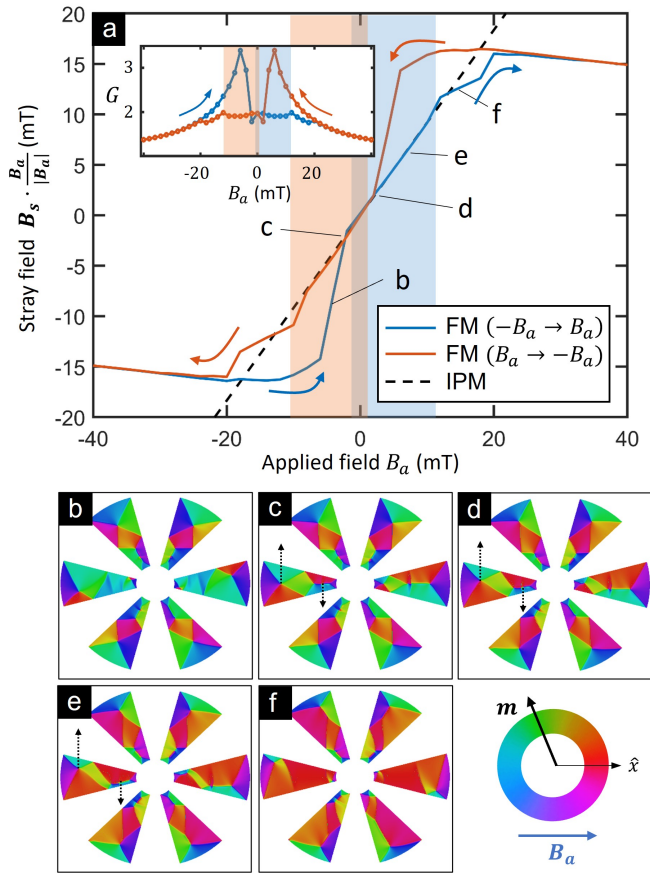


FIG. 2. Magnetic domain distribution in a six-petal MFC and the associated stray field. (a) Hysteresis loop of the stray field  $B_s$  emanating from the petals at the center of the device as a function of the applied field intensity  $B_a$ . Blue and orange lines are respectively for ascending and descending field sweeps. The dashed black line corresponds to an ideal paramagnetic material. Blue and orange highlighted regions show the range of applied magnetic fields for which there is a linear relation between  $B_0$  and  $B_a$  related to the displacement of the magnetic vortex cores and the domain walls. Inset: gain  $G$  as a function of the applied magnetic field. (b-f) Mapping of the magnetization at different applied magnetic fields. Panels (c-e) correspond to the linear regime with the dashed black arrows indicating the vortex displacement direction.

is reduced since a non-negligible part of the stray field at the inner tip of the petal spreads towards the out-of-plane direction and does not contribute to increasing the gain. This observation might suggest that there should exist an optimum thickness of the MFC in the range  $R_i < t < 2R_i$ , leading to a gain  $G \approx G_{max}/2$ , with  $G_{max} = R_o/R_i$  being the maximum possible gain obtained for an ideal magnetic metamaterial concentrator including IPM in combination with an ideal diamagnetic material [22]. For thicknesses below 100 nm, micromagnetic simulations (square symbols) departs from the predictions of the IPM model (circles), suggesting a reduction of the effective permeability of the device in very thin

structures related to the magnetic domain distribution.

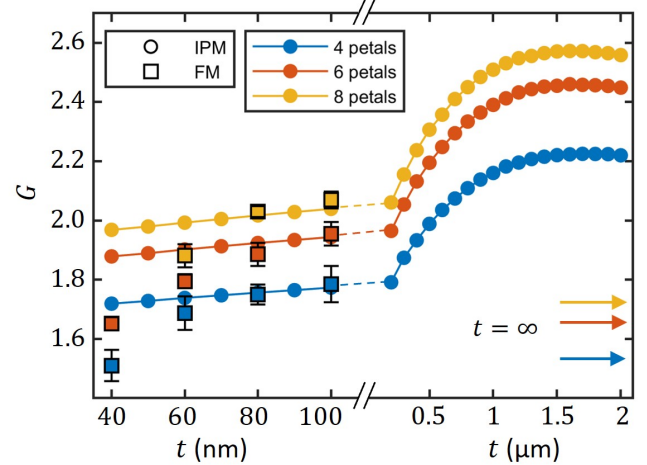


FIG. 3. Gain for devices with  $N_p = 4, 6$  and  $8$  as a function of the thickness  $t$ . The right-pointing arrows represent the gain for infinitely tall cylindrical devices (2D limit). Circles are obtained within the IPM model and square symbols correspond to micromagnetic simulations for a ferromagnetic device.

Fig. 3 also shows that the gain increases with the number of petals, similarly to what has been demonstrated for macroscopic concentrators [22]. However, simulations show that a structure made of  $N_p = 2$  outperforms the case  $N_p > 2$  reaching a maximum gain of about 2.2 (see Fig. 4). This is the case provided that the applied magnetic field is oriented along the bisector of the petals, as schematically shown in the upper inset of Fig. 4. For in-plane orientation angles  $\beta$  away from this optimum direction (corresponding to  $\beta = 0$ ), the gain is rapidly reduced. This highly anisotropic response requires careful orientation of the device and the knowledge beforehand of the direction of the magnetic field intended to be harvested or measured. From a technological application standpoint, it is convenient to increase the number of petals for the sake of rendering the device more isotropic, at the expense of slightly compromising the gain. Fig. 4 shows that an isotropic response is already achieved by increasing the number of petals to  $N_p = 4$ , irrespective of the thickness of the device. The fact that the gain becomes angular independent for  $N_p \geq 4$  has been confirmed for different angles of the petals and the same is expected when intercalating a perfect diamagnet between ferromagnetic petals. Additional simulations showing that the gain also depends on the opening angle  $\theta$  of the petals, with an optimum for  $\theta = \pi/N_p$ , are discussed in Supporting Information.

Let us now focus on the impact of the number of petals  $N_p$  on the gain of the device. As shown in Fig. 5(a), the higher  $N_p$ , the larger the mean gain  $\bar{G} = \frac{1}{2\pi} \int_0^{2\pi} G(\beta) d\beta$ , qualitatively following the trend predicted by the IPM approximation (dashed line). However, when the effect of

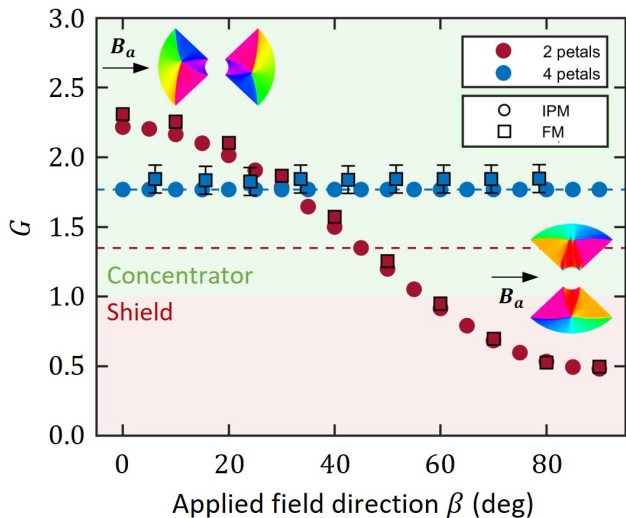


FIG. 4. Gain as a function of the in-plane magnetic field orientation  $\beta$  for  $N_p = 2$  and 4. Results from micromagnetic simulations (FM - squares) and IPM approximation (circles) show are qualitatively similar. The dashed line represents the angular-average gain  $\bar{G}$  for  $N_p = 2$ .

the magnetic domain distribution is included (squares), we observe that the computed gains depart from the IPM model for a larger number of petals. Moreover, a given structure can give rise to slightly different values of  $\bar{G}$  (maximum variation limited to 10%) depending on the magnetic domain configuration in the petals. This fact is illustrated in Fig. 5(b) where the stray field at the center of the device is shown as a function of the applied field for devices with 4 and 8 petals. In each petal, the domain arrangement is a combination of Landau, diamond and multiple cross-tie patterns. Interestingly, a higher gain is obtained when diamond rather than Landau or cross-tie patterns develop in the pair of petals aligned with the applied field. Furthermore, in the presence of diamond patterns the change of stray field intensity at the center of the device slightly deviates from the perfect linear relation  $B_s = (G - 1)B_a$ , with a slightly larger gain at low magnetic fields. As demonstrated for a rectangular strip of similar dimensions [24], there are no significant differences between the magnetic energies of cross-tie and diamond states for ideal samples and therefore the preferential magnetic configuration will mainly depend on the sample defects and magnetic history. In order to achieve optimal operation conditions, a constant gain is desired, which will in turn require the configuration of magnetic domains to be fixed. This could be done, for example, by introducing notches along the long sides of the petals to force the presence of domain walls and therefore promote the diamond states.

Although increasing the number of petals leads to a higher gain, it also reduces the range of the linear regime. This is shown in Fig. 5(c) where the annihilation field

$\mu_0 H_{an}$  (i.e. the applied field required to remove the flux-closure pattern and setting the limit of the linear regime) normalized by the thickness is plotted as a function of the number of petals for MFCs with different thicknesses. The annihilation field  $\mu_0 H_{an}$  is proportional to the demagnetization factor  $N_x$  as theoretically demonstrated for vortex expulsion in a magnetic thin disk [25]. This result suggests that a drastic reduction of the range of the linear regime is expected for thinner and longer petals as well as for a larger number of petals.

## B. Experimental results

In the previous section we have discussed the influence of several parameters on the theoretical gain of microscopic MFCs. Let us now compare these predictions based on micromagnetic simulations with the experimentally obtained  $G$  in microfabricated flower-like MFCs (see Section II B for details on the fabrication process and the device dimensions).

In order to evaluate the gain, it is necessary to be able to measure the in-plane component of the magnetic field at the center of the MFC. An elegant way to achieve this goal is to introduce a ferromagnetic sensor disk at the center of the MFC and to track the position of the magnetic vortex formed in the sensor as a function of the applied magnetic field. According to previous theoretical studies [25], the off-center displacement of the vortex core,  $\delta$ , should be linear with the applied magnetic field:

$$\delta(B_a) = \chi(0) \frac{R_d B_a}{\mu_0 M_s}, \quad (3)$$

where  $\chi(0)$  is the magnetic susceptibility at zero field,  $R_d$  is the radius of the disk and  $M_s$  its saturation magnetization. By measuring  $\delta$  for an isolated disk and for an identical disk surrounded by a MFC, we can deduce respectively  $B_a$  and  $B_s$ , and thus compute the gain  $G$ . Fig. 6(a) shows the displacement predicted by micromagnetic simulations for an isolated disk (blue circles) and a disk surrounded by a MFC (orange circles). These simulations have been performed for an applied magnetic field for which the MFC exhibits a linear response and sweeping from positive to negative fields. From the ratio of the slopes for the two lines in Fig. 6(a), a gain  $G \simeq 1.6$  is obtained. It is essential that the gap separating the sensor and the MFC,  $d_{gap}$ , exceeds a certain critical distance in order to avoid mutual dipolar interactions between the ferromagnetic sensor and the flux concentrator. Figure 6(b) shows the gain calculated from  $\delta$  as a function of the gap size. The black dashed line shows the theoretical gain without the sensor, or similarly for a sensor of insignificant size (i.e.  $R_d = 0$  and  $d_{gap} = R_i$ ). For  $d_{gap} < 0.1 \mu\text{m}$ , the sensor is strongly influenced by the MFC and does not host a vortex state, making it unsuitable for evaluating the gain. As a rule of thumb, a good accuracy of the sensor is obtained for  $d_{gap} \geq R_d$ . For the

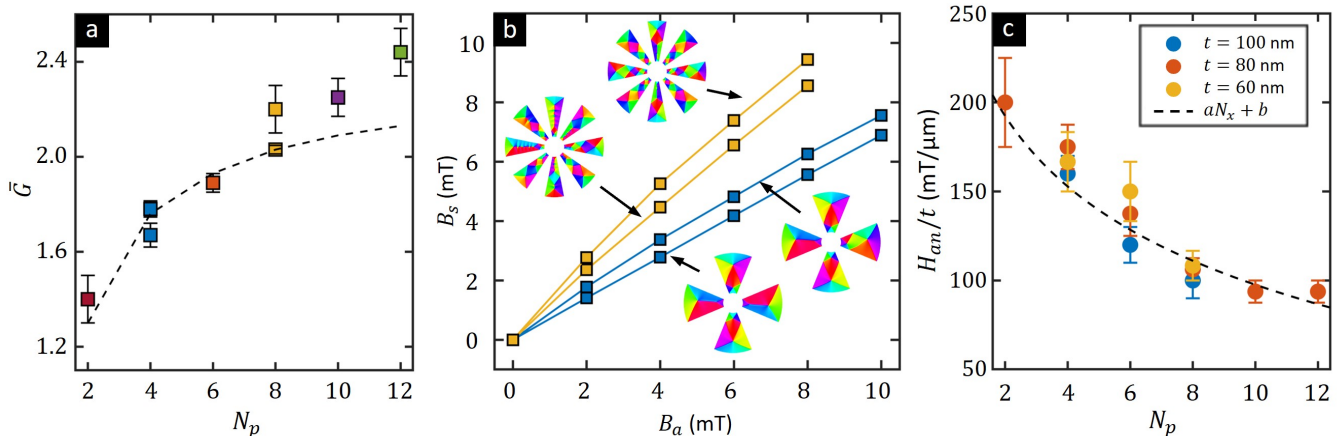


FIG. 5. (a) Evolution of the mean gain  $\bar{G}$  with the number of petals  $N_p$  for  $t = 80$  nm. Square symbols represent the predictions based on micromagnetic simulations whereas the IPM approximation is represented by the dashed line. For  $N_p = 4$  and  $8$  the two data points correspond to different configuration of magnetic domains. (b) Comparison of the stray field at the center of two identical devices exhibiting different magnetic domain configurations in each petal. The different configurations are obtained by slightly modifying the initial configuration before relaxing the structure. (c) Variation of the annihilation field normalized by the thickness as a function of  $N_p$ . The dashed black line shows the expected dependence assuming that  $\mu_0 H_{an} = aN_x + b$  ( $a$  and  $b$  are fitting parameters) where the demagnetization factor  $N_x$  is the one of a rectangular stripe with dimensions similar to the petal with the long axis aligned with the applied field [23].

sake of completeness, calculations have been performed varying  $R_i$  while fixing  $R_d$  and the other way around, with both results confirming the same trend. For computational reasons the simulated devices are limited in size ( $R_o = 5 \mu\text{m}$ ). However, the findings presented in Fig. 6(b) suggest that the gain can be efficiently probed for devices with various  $R_i$  and thus with larger dimensions (including the disk sensor radius), as long as the condition  $d_{gapd}$  is fulfilled.

Let us now discuss the experimental results, for which the MOKE microscopy has been used to track the core of the magnetic vortex in the disk-shaped sensor as a function of the in-plane applied magnetic field. Fig. 7(a) shows the obtained vortex displacement  $\delta$  for an isolated reference disk-shaped sensor (orange symbols) and a sensor surrounded by a four-petal MFC (blue symbols). The linear regime, for which the MFC is operational, is indicated by the blue region. Within this linear regime the vortex displacement rate  $d\delta/dB_a$  (represented by the colored dashed lines) is largest in the presence of the MFC, indicating that a more intense magnetic field is applied to the disk (i.e.  $G > 1$ ). Remarkably, the deviation from the constant gain approximation (dashed line) before entering the linear regime (between  $-0.2$  and  $0$  mT) has been already anticipated by the micromagnetic simulations as revealed by an abrupt increase of the gain in the inset of Fig. 2(a).

The gray scale in MOKE images is proportional to the local horizontal magnetization component, with dark (bright) areas representing negative (positive) magnetization. Based on this fact, we are able to determine the average reduced magnetization,  $m = M/M_s$ , for each in-

dividual petal. In Fig. 7(b) the orange (blue) line shows the average reduced magnetization for a petal aligned (perpendicular) to the applied magnetic field as extracted from the MOKE images shown in panels (c-h). The combination of these MOKE images and the hysteresis loops of individual petals allow us to confirm that the linear regime is conditioned by the formation of flux-closure patterns in all petals while its extension is limited by the existence of flux-closure state in the petals parallel to the applied field.

The fact that the microfabricated structures are one order of magnitude larger than the simulated ones, makes the magnetic field range for which the linear regime is experimentally observed substantially smaller compared to the simulations. Indeed, as presented in Fig. 5(c), the annihilation field is proportional to the demagnetization field, and the ratio of  $N_x$  for micromagnetic and experimental designs varies from 12 to 9 with an increasing number of petals.

By performing the same experiment on disks surrounded by MFCs with different number of petals (Fig. 8), and limiting the analysis to the linear regime, the trend predicted by the simulations nicely captures the experimental results. Fig. 8 shows a clear increase of the displacement rate due to the presence of the MFC, with a mean gain  $\bar{G}$  varying from 1 to 1.75 depending on  $N_p$ . As shown in the inset, the experimental results fairly well reproduce the micromagnetic predictions obtained for a smaller device. In an attempt to obtain a more quantitative comparison, we have also implemented the IPM model taking into account the actual size of the experimental device and a further reduction of the gain caused

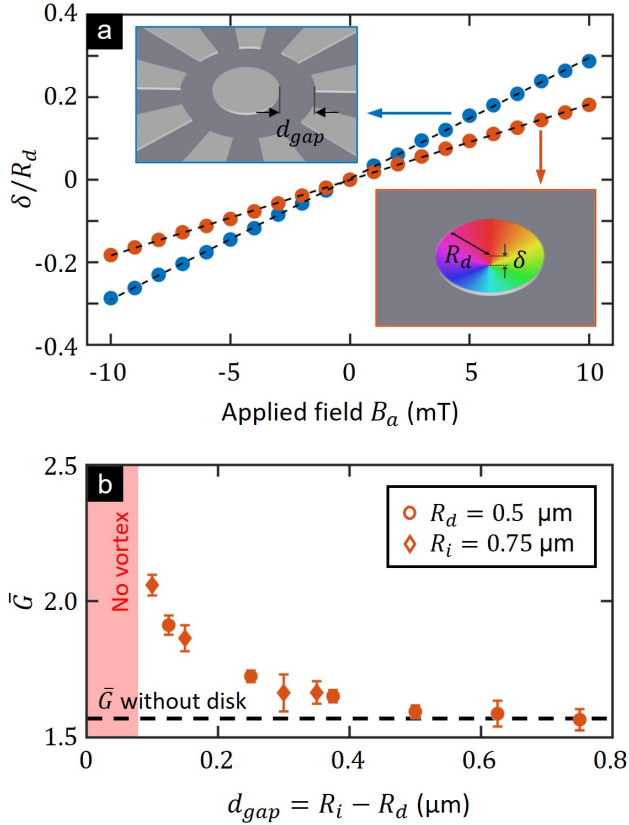


FIG. 6. (a) Micromagnetic simulation of the vortex core displacement with applied magnetic field in a 60-nm-thick disk isolated (blue) and surrounded by a six-petal MFC (orange). The insets illustrate the relevant geometrical parameters  $d_{gap}$ ,  $R_d$  and  $\delta$ . (b) Gain deduced from tracking the vortex core displacement in the disk sensor as a function of the gap  $d_{gap}$  separating the petals from the sensor. The sensor is impractical for  $d_{gap} < 0.1 \mu\text{m}$  and its read-out is reliable only for  $d_{gap} > 0.4 \mu\text{m}$ . The black dashed line shows the theoretical gain without the central disk. Simulations have been done with  $R_o = 4R_i$ .

by the presence of magnetic domains (see Supporting Information). There are however, several ingredients which can affect the efficiency of the device that are not considered in the numerical model. Namely, defects inherent to the fabrication process, the Py grain structure, the formation of a magnetic dead layer, or the presence of pinning sites. Results reported in Fig. 8 have been obtained on MFCs with radii  $R_o = 5R_i = 80 \mu\text{m}$ . For the sake of completeness, the same experiment was performed on devices with smaller dimensions, leading to the same conclusion. Results are reported in Supporting Information.

In Fig. 8 two sets of blue datapoints are depicted for the two-petal MFC, evidencing the anisotropic response of the device when the applied in-plane magnetic field is parallel ( $\beta = 0$ ) or perpendicular ( $\beta = \pi/2$ ) to the

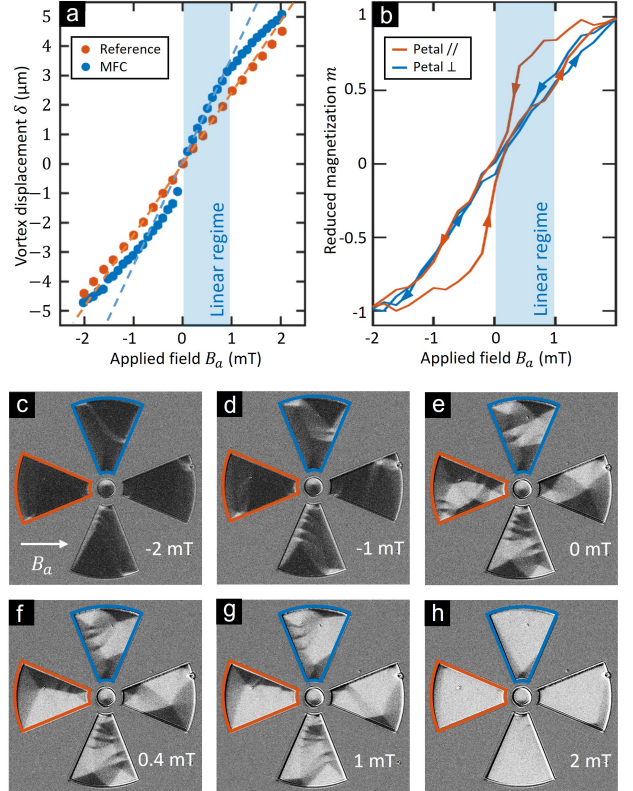


FIG. 7. (a) Experimentally determined relative vortex core position in a sensor-disk with radius  $R_d = d_{gap} = R_i/2$  surrounded by a four-petal MFC with radius  $R_o = 5R_i = 80 \mu\text{m}$  (blue symbols) and for an isolated sensor-disk (orange symbols). The dashed lines are linear fits in the linear regime. (b) Hysteresis curves corresponding to a single petal obtained from contrast change in MOKE images partially presented in panels (c-h). The color code of the curves in panel (b) corresponds to the petal indicated in panels (c-h).

petals. The mean gain over a complete rotation of the device as calculated following the same method used for Fig. 4 leads to a negligible concentration power, i.e.  $\bar{G} \simeq 1$ . A more detailed angular dependence measurement is summarized in Fig. 9 where a cosinusoidal variation of the gain is obtained for a two-petal MFC whereas a four-petal MFC exhibits an isotropic behaviour, in good agreement with the numerical modeling.

#### IV. CONCLUSION

In summary, we have presented an in-depth analysis scrutinizing the possibility to use ferromagnetic-based metasurfaces to concentrate magnetic flux at the micrometer scale. Firstly, we have demonstrated that the performance of the studied magnetic flux concentrators depends on the thickness of the device, with an optimal thickness  $R_i < t < 2R_i$ . We have also shown that the properties predicted for macroscopic devices studied in Ref. [15] concerning the effect of petal number and di-



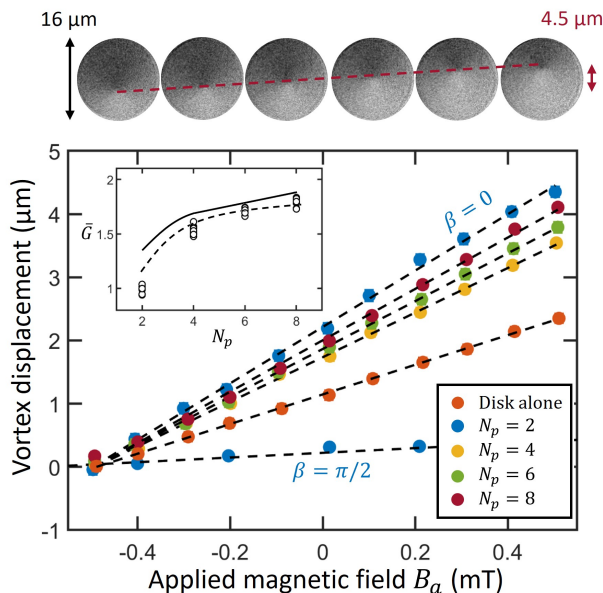


FIG. 8. Experimentally determined effect of the number of petals on the vortex displacement rate compared to a reference isolated disk (orange). The two sets of datapoints for the  $N_p = 2$  MFC (blue) correspond to the cases where the applied in-plane magnetic field is parallel and perpendicular to the petals, respectively. MOKE images at the top of the figure show the change of vortex core position in the sensor surrounded by the 8-petal device. The inset shows the measured mean gain  $\bar{G}$  as a function of  $N_p$  for a large batch of different devices with  $R_o = 80 \mu\text{m}$  (black circles). The upper line shows the theoretical result deduced from micromagnetic simulations for a device substantially smaller than that experimentally measured. The lower dashed line corresponds to IPM predictions for the correct sample size and including a further reduction of the gain caused by the presence of magnetic domains.

dimension, as well as the isotropic response of the concentrator, are reproduced in microscopic devices. Secondly, we have demonstrated through micromagnetic simulations that the non-linear response of the ferromagnet limits the range of magnetic fields for which the concentrator can operate with a constant gain greater than 1. This range corresponds to the regime of stabilization of flux-closure patterns in each petal of the MFC and can be tuned by modifying the demagnetization factor of the petals. Lastly, we experimentally confirm the theoretical predictions for devices with an outer radius of 40 and 80  $\mu\text{m}$ . We demonstrate that the gain of on-chip MFCs can be obtained by imaging domains with MOKE microscopy and by tracking the displacement of a magnetic vortex core formed in a FM disk placed at the center of the MFC. Our results prove that an isotropic response is obtained with a MFC composed of at least four petals and the concentration gain measured experimentally follows the predicted trend regarding the number of petals. Several routes could be explored to further improve the performance of MFCs. In particular, a closer

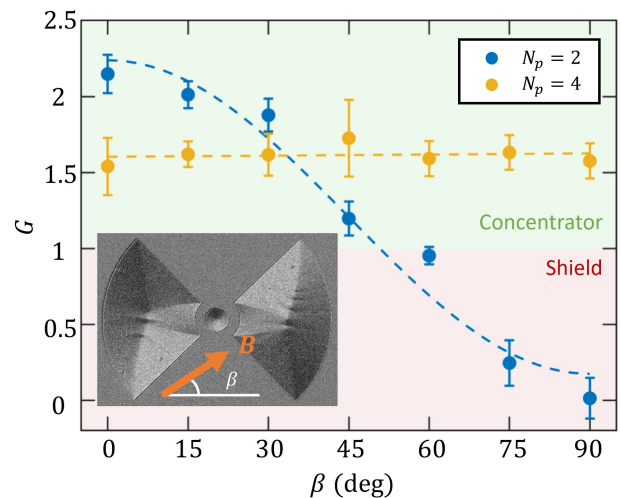


FIG. 9. Variation of the gain as a function of the in-plane magnetic field direction  $\beta$  as illustrated in the inset. The in-plane anisotropy observed with a two-petal MFC vanishes for a four-petal concentrator.

look should be taken at how the domain arrangement can improve the efficiency of the metasurfaces. Further experimental aspects deserve to be investigated, such as the use of magnetoresistive sensors, the possibility to introduce different ferromagnetic materials for the MFC and the sensor, and adapting the shape of the sensor to exploit its shape anisotropy. **As a final remark we would like to point out that even though only DC magnetic fields have been investigated in this work, the proposed MFCs should be equally suited for higher frequency applications up to hundreds of MHz. The reason for this broadband resilience is manifold. Firstly, because of the MFC thin film geometry, losses associated to eddy currents are negligible [26]. Secondly, if external magnetic field intensities restricted to the MFC linear regime are considered, the dynamic response of the petals consists in domain walls displacements which are expected to exhibit little lag under external excitation of few hundreds of MHz in Py microstructures [27]. Thirdly, magnetic losses arising from the ferromagnetic resonance are expected at substantially higher frequencies (of the order of GHz). A more quantitative and accurate determination of the impact of geometrical and material's parameters on the cut-off frequency limiting the operational spectrum of the MFC deserves further theoretical and experimental investigations.**

## V. ACKNOWLEDGEMENT

This work was supported by the Fonds de la Recherche Scientifique - FNRS under the programs PDR T.0204.21 and CDR J.0176.22, EraNet-CHIST-ERA R.8003.21, the Spanish Ministry of Science and Innovation MCIN/AEI /10.13039/501100011033/ through CHIST-ERA

PCI2021-122028-2A and PCI2021-122083-2A cofinanced by the European Union Next Generation EU/PRTR and HTSUPERFUN PID2021-124680OB-I00 cofinanced by ERDF “A way of making Europe”, the Research Foundation and by COST (European Cooperation in Science and Technology) [www.cost.eu] through COST Action SUPERQUMAP (CA 21144). Access to the CEITEC Nano

Research Infrastructure was supported by the Ministry of Education, Youth and Sports (MEYS) of the Czech Republic under the project CzechNanoLab (LM2018110). JAA and VU acknowledge the support from the TACR EraNet CHIST-ERA project MetaMagIC TH77010001. EF and AVS gratefully acknowledge B. Vanderheyden for the fruitful discussions and proofreading.

- 
- [1] IEA, Digitalisation and energy (2017), license: CC BY 4.0.
- [2] S. Tumanski, *Handbook of magnetic measurements*, edited by H. H. B. Jones (CRC press, 2011).
- [3] C. Zheng, K. Zhu, S. C. De Freitas, J.-Y. Chang, J. E. Davies, P. Eames, P. P. Freitas, O. Kazakova, C. Kim, C.-W. Leung, *et al.*, Magneto-resistive sensor development roadmap (non-recording applications), *IEEE Transactions on Magnetics* **55**, 1 (2019).
- [4] P. M. Drljača, F. Vincent, P.-A. Besse, and R. S. Popović, Design of planar magnetic concentrators for high sensitivity hall devices, *Sensors and Actuators A: Physical* **97**, 10 (2002).
- [5] P. Leroy, C. Coillot, A. F. Roux, and G. M. Chanteur, High magnetic field amplification for improving the sensitivity of hall sensors, *IEEE Sensors Journal* **6**, 707 (2006).
- [6] A. Edelstein, G. Fischer, M. Pedersen, E. Nowak, S. F. Cheng, and C. Nordman, Progress toward a thousandfold reduction in  $1/f$  noise in magnetic sensors using an ac microelectromechanical system flux concentrator, *Journal of Applied Physics* **99**, 08B317 (2006).
- [7] Z. Marinho, S. Cardoso, R. Chaves, R. Ferreira, L. Melo, and P. Freitas, Three dimensional magnetic flux concentrators with improved efficiency for magneto-resistive sensors, *Journal of Applied Physics* **109**, 07E521 (2011).
- [8] X. Sun, L. Jiang, and P. W. Pong, Magnetic flux concentration at micrometer scale, *Microelectronic Engineering* **111**, 77 (2013).
- [9] Y. Bi, X. M. Zhang, and W. J. Wang, Design study of trapezoid-shaped magnetic flux concentrator for axial amplification characteristics, in *Applied Mechanics and Materials*, Vol. 875 (Trans Tech Publ, 2018) pp. 77–83.
- [10] V. Annapureddy, H. Palneedi, G.-T. Hwang, M. Peddigari, D.-Y. Jeong, W.-H. Yoon, K.-H. Kim, and J. Ryu, Magnetic energy harvesting with magnetoelectrics: an emerging technology for self-powered autonomous systems, *Sustainable Energy & Fuels* **1**, 2039 (2017).
- [11] H. Song, D. R. Patil, W.-H. Yoon, K.-H. Kim, C. Choi, J.-H. Kim, G.-T. Hwang, D.-Y. Jeong, and J. Ryu, Significant power enhancement of magneto-mechano-electric generators by magnetic flux concentration, *Energy & Environmental Science* **13**, 4238 (2020).
- [12] X. Zhang, Y. Bi, G. Chen, J. Liu, J. Li, K. Feng, C. Lv, and W. Wang, Influence of size parameters and magnetic field intensity upon the amplification characteristics of magnetic flux concentrators, *AIP Advances* **8**, 125222 (2018).
- [13] A. Sanchez, C. Navau, J. Prat-Camps, and D.-X. Chen, Antimagnets: controlling magnetic fields with superconductor–metamaterial hybrids, *New Journal of Physics* **13**, 093034 (2011).
- [14] C. Navau, J. Prat-Camps, and A. Sanchez, Magnetic energy harvesting and concentration at a distance by transformation optics, *Physical Review Letters* **109**, 263903 (2012).
- [15] J. Prat-Camps, C. Navau, and A. Sanchez, Experimental realization of magnetic energy concentration and transmission at a distance by metamaterials, *Applied Physics Letters* **105**, 234101 (2014).
- [16] C. Navau, R. Mach-Batlle, A. Parra, J. Prat-Camps, S. Laut, N. Del-Valle, and A. Sanchez, Enhancing the sensitivity of magnetic sensors by 3d metamaterial shells, *Scientific Reports* **7**, 1 (2017).
- [17] D. P. Arnold, Review of Microscale Magnetic Power Generation, *IEEE Transactions on Magnetics* **43**, 3940 (2007).
- [18] A. Vansteenkiste, J. Leliaert, M. Dvornik, M. Helsen, F. Garcia-Sanchez, and B. Van Waeyenberge, The design and verification of mumax3, *AIP Advances* **4**, 107133 (2014).
- [19] J. Leliaert, B. Van de Wiele, A. Vansteenkiste, L. Laurson, G. Durin, L. Dupré, and B. Van Waeyenberge, Current-driven domain wall mobility in polycrystalline permalloy nanowires: A numerical study, *Journal of Applied Physics* **115**, 233903 (2014).
- [20] A. Barrera, E. Fourneau, S. Martín, J. M. Batllori, J. Alcalá, L. Balcells, N. Mestres, N. D. Nguyen, A. Sanchez, A. Silhanek, and A. Palau, Tunable perpendicular magneto-resistive sensor driven by shape and substrate induced magnetic anisotropy, *Advanced Sensor Research* 10.1002/adsr.202200042 (2022).
- [21] I. Soldatov and R. Schäfer, Selective sensitivity in kerr microscopy, *Review of Scientific Instruments* **88**, 073701 (2017).
- [22] J. Prat-Camps, A. Sanchez, and C. Navau, Superconductor–ferromagnetic metamaterials for magnetic cloaking and concentration, *Superconductor Science and Technology* **26**, 074001 (2013).
- [23] A. Aharoni, Demagnetizing factors for rectangular ferromagnetic prisms, *Journal of Applied Physics* **83**, 3432 (1998).
- [24] W. Rave and A. Hubert, Magnetic ground state of a thin-film element, *IEEE Transactions on Magnetics* **36**, 3886 (2000).
- [25] K. Y. Guslienko, V. Novosad, Y. Otani, H. Shima, and K. Fukamichi, Field evolution of magnetic vortex state in ferromagnetic disks, *Applied Physics Letters* **78**, 3848 (2001).
- [26] I. Iakubov, A. Lagarkov, A. Osipov, S. Maklakov, K. Rozanov, I. Ryzhikov, and S. Starostenko, A laminate of ferromagnetic films with high effective permeability at high frequencies, *AIP Advances* **4**, 107143 (2014).

- [27] K. W. Chou, A. Puzic, H. Stoll, G. Schütz, B. Van Waeyenberge, T. Tyliczszak, K. Rott, G. Reiss, H. Brückl, I. Neudecker, *et al.*, Vortex dynamics in coupled ferromagnetic multilayer structures, *Journal of applied physics* **99**, 08F305 (2006).